8976–8989 *Nucleic Acids Research, 2016, Vol. 44, No. 18* *Published online 24 June 2016*
doi: 10.1093/nar/gkw576

Box C/D sRNA stem ends act as stabilizing anchors for box C/D di-sRNPs

W. S. Vincent Yip[1], Hideki Shigematsu[2,3], David W. Taylor[4,5] and Susan J. Baserga[1,6,7,*]

[1]Department of Molecular Biophysics and Biochemistry, Yale University, New Haven, CT 06520, USA, [2]Department of Cellular and Molecular Physiology, Yale University, New Haven, CT 06520, USA, [3]RIKEN Center for Life Science Technology, Yokohama, Kanagawa 230-0045, Japan, [4]Department of Molecular and Cell Biology, University of California, Berkeley, CA 94720, USA, [5]California Institute for Quantitative Biosciences, University of California, Berkeley, CA 94720, USA, [6]Department of Genetics, Yale University, New Haven, CT 06520, USA and [7]Department of Therapeutic Radiology, Yale University, New Haven, CT 06520, USA

Received April 09, 2016; Revised June 14, 2016; Accepted June 15, 2016

ABSTRACT

Ribosomal RNA (rRNA) modifications are essential for ribosome function in all cellular organisms. Box C/D small (nucleolar) ribonucleoproteins [s(no)RNPs] catalyze 2′-*O*-methylation, one rRNA modification type in Eukarya and Archaea. Negatively stained electron microscopy (EM) models of archaeal box C/D sRNPs have demonstrated the dimeric sRNP (di-sRNP) architecture, which has been corroborated by nuclear magnetic resonance (NMR) studies. Due to limitations of the structural techniques, the orientation of the box C/D sRNAs has remained unclear. Here, we have used cryo-EM to elucidate the sRNA orientation in a *M. jannaschii* box C/D di-sRNP. The cryo-EM reconstruction suggests a parallel orientation of the two sRNAs. Biochemical and structural analyses of sRNPs assembled with mutant sRNAs indicate a potential interaction between the sRNA stem ends. Our results suggest that the parallel arrangement of the sRNAs juxtaposes their stem ends into close proximity to allow for a stabilizing interaction that helps maintain the di-sRNP architecture.

INTRODUCTION

Ribosome biogenesis, the manufacture of ribosomes for protein synthesis, is a fundamental cellular process in all three domains of life. To generate a correctly folded and fully functional ribosome, the pre-ribosomal RNA (pre-rRNA) undergoes a large number of chemical modifications (1–5). In Eukarya and Archaea, the two major types of pre-rRNA modifications are pseudouridylations and 2′-*O*-methylations of the ribose moiety (1,6). These modifications are critical as the global or even local removal of them leads to reduction in growth or developmental defects (2–4,7–9). Many of the modifications are located in functionally important and evolutionarily conserved regions of the ribosome, including the intersubunit bridge, the peptidyl transferase center and the decoding center (1–4). Furthermore, the number of modifications increases with the complexity of the organisms (10–14). In Archaea, the number of modifications also positively correlates with their growth temperature (15). Taken together, pseudouridylation and 2′-*O*-methylation of pre-rRNAs are important for both the function and structural stability of ribosomes.

In Eukarya and Arcahea, 2′-*O*-methylations are carried out by specialized guide RNP complexes (16–18). These RNPs are known as box C/D small nucleolar RNPs (snoRNPs) in Eukarya. In Archaea, they are known as box C/D small RNPs (sRNPs) because of the absence of nucleoli (19). The core components of an archaeal box C/D sRNP are known, and a catalytically active archaeal box C/D sRNP has been reconstituted *in vitro* (19,20). One such component is the box C/D sRNA (20–26), which houses the box C (RUGAUGA, where R is a purine) and D (CUGA) elements close to the terminal stem that form the kink-turn structural element (Figure 1A) (27–30). In addition, the box C/D sRNA also contains the degenerate box C' and D' elements, which, together with the internal loop, form the kink-loop structural element (31). Sandwiched between the box C/D and box C'/D' elements are two single-stranded sequences known as the guide sequences. Each guide sequence base pairs with the target RNA sequence in the pre-rRNA substrate (16–19). Through base-pairing, the guide sequences confer specificity to the 2′-*O*-methyl transfer reactions such that the substrate is methylated at a site that is exactly five nucleotides upstream (n+5 rule) of the box D or D' (16,17,32).

In addition to the sRNA, an archaeal box C/D sRNP also contains three proteins: L7Ae (NHP2L1, formerly 15.5K, in humans), Nop5 (Nop56/58 in humans) and fibrillarin (19). L7Ae is an RNA binding protein that

*To whom correspondence should be addressed. Tel: +1 203 785 4618; Fax: +1 203 785 6404; Email: susan.baserga@yale.edu

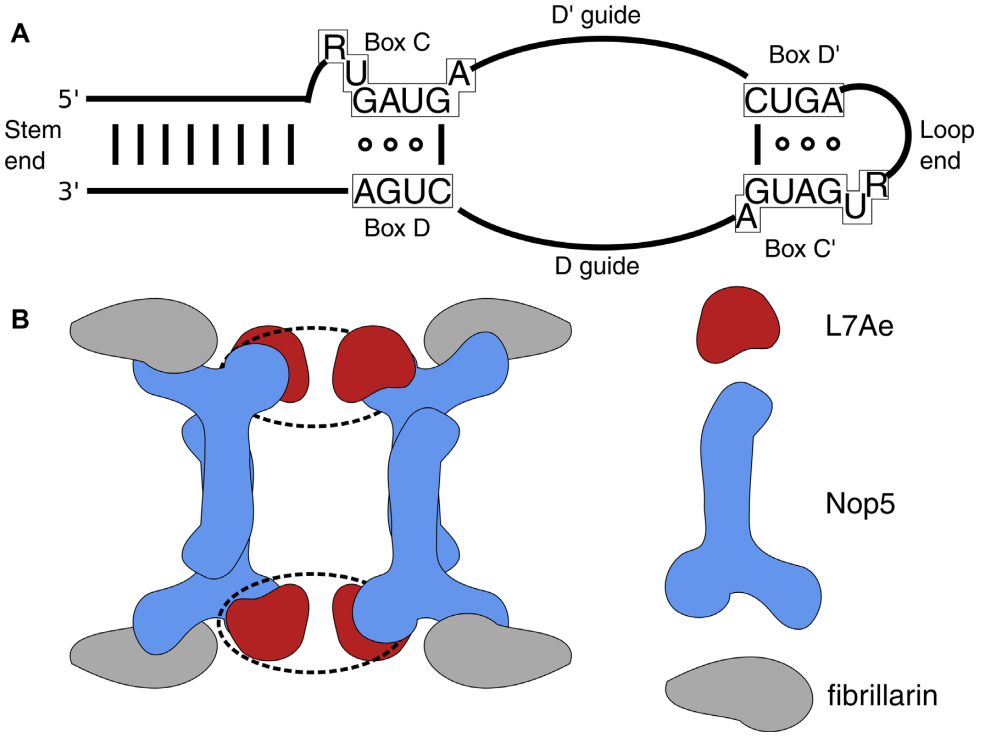

Figure 1. The dimeric sRNP model. (**A**) Schematic of an archaeal box C/D sRNA. The RNA contains a stem end, formed by the 5′ and 3′ termini, and a loop end. The consensus elements box C and D form the kink-turn structural element, and the box C' and D' form the kink-loop structure element. The two single-stranded regions enveloped by the consensus elements are the guide sequences that base pair with the substrates. (**B**) Schematic of the dimeric sRNP model proposed by (45). L7Ae is indicated in red, Nop5 in blue, fibrillarin in gray. The dotted ellipses represent the proposed locations and orientations of the two sRNA copies.

recognizes the kink-turn and kink-loop structures of the box C/D sRNAs (19,27,33–37). Fibrillarin contains an *S*-adenosylmethionine (SAM) binding pocket and is the catalytic protein that performs the chemistry of 2′-*O*-methylation using SAM as the methyl group donor (7,19,38–41). Nop5 binds the sRNA kink-turn and kink-loop structures through its C-terminal domain (CTD) and fibrillarin through its N-terminal domain (NTD) (39,41–45). It also dimerizes with itself through its coiled coil domain, thereby linking the L7Ae-sRNA complex with fibrillarin (39,41–44,46,47).

Recent structural studies of archaeal box C/D sRNPs have presented two different structural models. A 3-dimensional (3D) reconstruction of the *M. jannaschii* box C/D sRNP obtained by negatively stained electron microscopy (EM) from our laboratory proposed a dimeric sRNP (di-sRNP) model (Figure 1B), with four copies of each of the core proteins, linked together by two copies of the box C/D sRNAs (45). In contrast, a crystal structure of *S. solfataricus* box C/D sRNP presented a monomeric sRNP (mono-sRNP) model, with only two copies of each of the core proteins and one copy of the box C/D sRNA (42). Our subsequent biochemical and EM studies of additional box C/D sRNPs from various archaeal species have demonstrated that the mono-sRNP is a result of the use of an artificial, synthetic sRNA that lacks an important loop structure near the box C'/D' element (Figure 1A) (48). Extensive structural studies using nuclear magnetic resonance (NMR) and biochemical studies have also arrived at a di-sRNP architecture (49,50). Therefore, there is ample biochemical and structural evidence that archaeal box C/D sRNPs adopt a di-sRNP structure upon *in vitro* assembly with a natural box C/D sRNA.

While the negatively stained EM and NMR structures have clearly demonstrated the relative orientation of the core proteins in box C/D di-sRNPs, the orientation of the box C/D sRNAs has remained elusive. In the negatively stained EM structure, the density of the box C/D sRNAs cannot be resolved (45,48). This is likely a result of staining artifacts that render RNA undetectable (51–53). The NMR structural model was not generated *de novo* due to the limitations of conventional NMR in determining the structure of a large macromolecular complex (~400 kDa) (49). Instead, the derivation of the NMR structural model relied heavily on previously published crystal structures of incomplete box C/D sRNP fragments. Since the NMR-based structural model is not a *de novo* structure of the entire box C/D di-sRNP, it may not depict the correct assignment of the orientation of the box C/D sRNAs.

To circumvent the limitations of negatively stained EM, we used cryo-EM to determine the 3D reconstruction of the *M. jannaschii* box C/D di-sRNP at 9.0Å resolution. The cryo-EM reconstruction reveals a density that is not present in the previously published negatively stained EM reconstructions, which we propose corresponds to the box C/D sRNAs. We hypothesize that the additional density corresponds to the sRNAs that penetrate the core of the di-sRNP and are exposed on both its front and back faces. Dock-

ing of the crystal structures of the box C/D sRNP core proteins and the kink-turn RNAs into the cryo-EM volume suggests that the two sRNAs are oriented in a parallel fashion and reveals a potential interaction between their stem ends. Indeed, native polyacrylamide gel electrophoresis (PAGE) shows that mutant sRNAs with disrupted stem ends assemble into di-sRNPs less efficiently. Moreover, native PAGE, size exclusion chromatography (SEC) and EM analysis demonstrate that a fusion di-sRNA, composed of two sRNAs fused at the stem ends, is able to assemble into a di-sRNP, further supporting the notion of stem end interactions between the sRNAs. Taken together, these results suggest a model in which the two sRNAs orient in a parallel fashion in the box C/D di-sRNP to facilitate the interaction of their stem ends that stabilize the di-sRNP architecture.

MATERIALS AND METHODS

Protein expression and purification

Expression and purification of full-length *M. jannaschii* L7Ae (13.0 kD), Nop5 (amino acids 1–367, 42.2 kD) and full-length fibrillarin with a N-terminal FLAG-tag (27.8 kD) were performed as described in (45) and (48).

In vitro transcription of wildtype and mutant sRNAs

Stem mismatch and truncation mutants were created from the pUC19 vector containing the sR8 sRNA gene with a 5′ T7 RNA polymerase promoter from (45) with oligonucleotides in Supplementary Table S1A using the Change-IT™ multiple mutation site directed mutagenesis kit (Affymetrix), according to the manufacturer's instructions. These constructs were used to generate linearized T7-promoter-containing templates using oligonucleotides in Supplementary Table S1B by the polymerase chain reaction (PCR). The templates were used in *in vitro* transcription as described in (45,47,48) to generate wildtype (WT) and stem truncation and mismatch mutant sRNAs. The *in vitro* transcribed WT sR8 sRNA has a theoretical molecular mass of 21.8 kD.

In vitro transcription and UREA-PAGE purification of di-sR8 sRNAs

di-sR8 T7 sense and di-sR8 T7 anti-sense oligonucleotides (Supplementary Table S1C) were annealed at 95°C for 2 min and allowed to cool down to room temperature slowly in 26 min in a thermal cycler to generate a DNA template containing the T7 promoter sequence. The template was used in *in vitro* transcription as described in (45) to generate di-sR8 sRNA. The transcription product was electrophoresed in a 5% UREA-PAGE (5% polyacrylamide, 7.5 M urea, 89 mM Tris-base, 89 mM Boric Acid, 2 mM EDTA at pH 8.3). The gel was visualized using UV shadowing and the gel band containing the full length transcription product was excised. The gel band was crushed and soaked in a buffer containing 50 mM Tris-HCl at pH 7.5 and 300 mM sodium acetate at 4°C overnight with nutation. The gel pieces were removed by centrifugation at 5000 g for 1 min followed by filtration with a 0.4 μm syringe filter. The purified di-sR8 sRNA was precipitated with ethanol at −80°C overnight and stored as precipitant until use.

sRNP assembly

sRNPs were assembled as described in (45) with the exception that the di-sR8 sRNP was assembled at lower protein and sRNA concentrations (2.63 μM of di-sR8 and 6.5 μM of L7Ae, Nop5 and fibrillarin).

Size exclusion chromatography

Five hundred microliters of WT sR8 or di-sR8 was purified using Superose 6 10/300 GL with buffer G0 (20 mM HEPES at pH 7.5, 300 mM NaCl and 1.5 mM $MgCl_2$). Fractions of 500 μl were collected. For the WT sR8 sRNP, the fractions were analyzed by SDS-PAGE followed by silver staining and northern blotting (Figure 2B) as described in (45). The peak fraction was also analyzed by electron microscopy and by native PAGE (as below).

Native PAGE analysis

Thirty microliters of sRNPs assembled with WT sR8 and sR8 stem truncation and mismatch mutants were loaded onto a 6% native PAGE gel and resolved by electrophoresis as described in (48). The gels were stained by ethidium bromide and silver staining to visualize the sRNPs. sRNAs from 10 μl of each assembled sRNP solution were also extracted and analyzed by northern blot and probed by a radiolabled oligonucleotide in Supplementary Table S1D as described in (45) to quantify the amount of sRNA present in each gel lane. These analyses were performed three times and the gel intensity was quantified using ImageJ software package. Statistical analysis was performed using the Graphpad Prism software package.

Peak fractions (fractions 5–7) from size exclusion chromatography of di-sR8 sRNP were combined and concentrated to 50 μl using Pierce™ protein concentrators, PES, 10K MWCO. Thirty microliters of the concentrated fraction and 4 μl of the un-concentrated peak fraction (fraction 5) of the WT sR8 sRNP were loaded onto a 6% Native PAGE gel and resolved and stained as described above.

In vitro methylation activity assays

Methylation activity assays were performed as described in (45,48). Briefly, to each 20 μl of sRNP, 5 μl of reaction mixture was added so that the final concentrationt for the reaction contained 9 μM of substrate, 27 μM of non-radioactive SAM and 0.795 μCi of *S*-adenosyl-L-[methyl-^{3}H]-methionine (^{3}H-SAM) in a buffer of 20 mM HEPES (pH 7.5), 500 mM NaCl, 10% glycerol and 1.5 mM $MgCl_2$. The reaction was incubated at 70°C for 30 min and the entirety of the reaction was spotted on a double layer of Whatman 3MM and DE83 filters. The DE83 filter was washed with 5 ml 10% trichloroacetic acid (TCA) once, 5 ml 5% TCA three times and 5 ml 100% ethanol three times. The filter was dried and the incorporated ^{3}H-methyl groups were quantitated with a liquid scintillation counter. Each reaction was done in triplicate and statistical analysis was performed using a two-tailed *t*-test in the Graphpad Prism software package. Supplementary Table S1E contains the sequences of the substrates used.

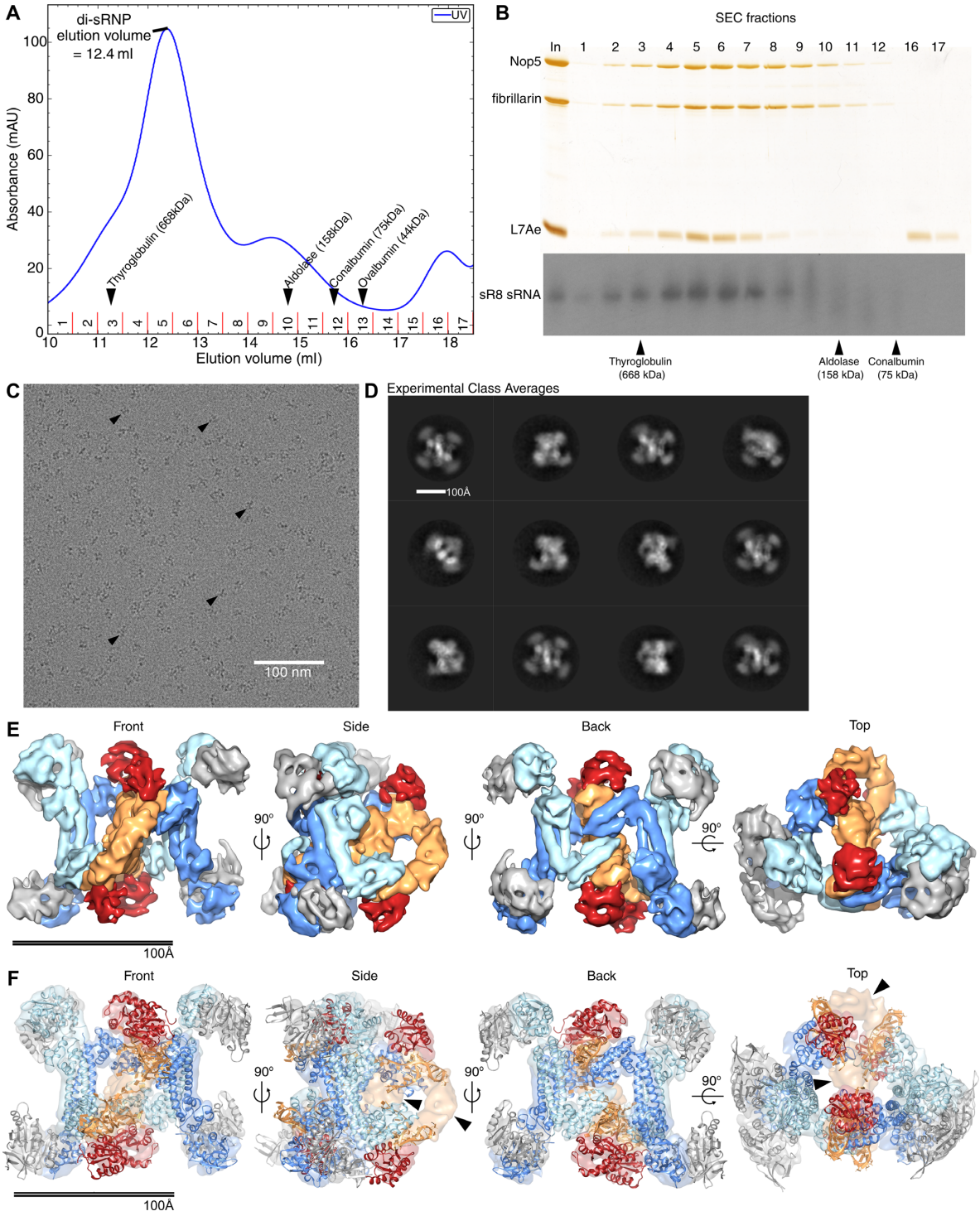

Figure 2. Purification and visualization of *M. jannaschii* box C/D di-sRNP by cryo-EM. (**A**) Size-exclusion chromatography (SEC) of *M. jannaschii* box C/D sRNP. The assembled sRNP elutes at peak fractions 5 and 6, corresponding to an elution volume of 12.4 ml. Arrowheads indicate the elution volumes of various sizing standards (thyroglobulin, aldolase, conalbumin and ovalbumin). (**B**) **Upper panel**: SDS-PAGE analysis of selected fractions from SEC. 'In' corresponds to 2% input of the SEC. **Lower panel**: a northern blot showing the presence of sRNA in the corresponding fractions. All three proteins and the sRNA co-elute in fractions 5 and 6, corresponding to the peak fractions in the SEC. Arrowheads below the panel indicate the peak fractions at which various sizing standards (thyroglobulinn, aldolase and conalbumin) elute. (**C**) An aligned and averaged electron micrograph of *M. jannaschii* box C/D sRNP in vitreous ice. Each arrowhead indicates a single particle of a sRNP molecule. Scale bar is 100 nm. (**D**) Twelve representative cryo-EM 2D classes of *M. jannaschii* box C/D sRNP. Scale bar is 100Å. (**E**) 3D cryo-EM reconstruction of *M. jannaschii* box C/D sRNP, rotated around the y-axis and the x-axis, at 9.0Å resolution. The map is segmented based on the identities of the corresponding protein or sRNA densities. L7Ae is in red, Nop5 in blue and light blue, fibrillarin in gray, sRNA in light brown. Scale bar is 100Å. (**F**) Docking of crystal structures of *P. furiosus* proteins and kink-turn RNAs in the EM volume [PDB ID: 2NNW and 3NVI (41,44)]. Color code is the same as in E. The arrowheads in the side and top views indicate the electron densities unaccounted for by crystal structures and are suggestive of the sRNA locations.

Negatively stained electron microscopy specimen preparation

A C-Flat holey carbon grid (Electron Microscopy Sciences) layered with a carbon support film was glow-discharged by a Solarus^{TM} plasma cleaner. Five microliters of either the concentrated peak fractions of di-sR8 sRNP or the un-concentrated peak fraction of WT sR8 sRNP were applied to the grid. After 30 s of adsorption, the grid was stained with 2% uranyl formate solution for 30 s. Excess staining solution was removed by blotting with filter papers, and the grid was air dried.

Cryo-electron microscopy specimen preparation

Two and a half microliters of the un-concentrated peak fraction of WT sR8 sRNP were applied to a glow-discharged C-Flat holey carbon grid layered with a carbon support film as above. After 30 s of adsorption at 8°C and 100% relative humidity, the grid was plunge frozen in liquid ethane using the Vitrobot MarkIII(FEI) with a blotting time of 5 s and blot offset of −1 mm. The frozen specimen was stored in liquid nitrogen until use.

Electron microscopy image acquisition

All specimens were examined using a Tecnai FEI F20 electron microscope equipped with a field-emission gun operated at 200keV. Images of negatively stained specimens were recorded at a nominal magnification of 50 000x using a GATAN Ultrascan 4k × 4k CCD camera with an exposure dose of 30 $e^{-}Å^{-2}$ and a defocus range between −0.6 μm and −1.2 μm. These micrographs had a pixel size of 1.88Å. Images of frozen hydrated specimens were recorded at a nominal magnification of 29 000x using a GATAN K2 Summit direct detection camera in counting mode at a dose rate of 8 $e^{-}pixel^{-1}s^{-1}$ with a defocus range between −2.5 μm and −4 μm. Movies were collected such that the total exposure dose was 30 $e^{-}Å^{-2}$. These micrographs had a pixel size of 1.25Å.

Image Processing

Movie frames collected on the direct detector were aligned and averaged using MATLAB scripts written by Shigematsu and Sigworth (54). Contrast transfer functions (CTF) of all averaged micrographs and CCD micrographs were estimated using CTFFIND3 (55). Particles were either manually selected from the negatively stained EM CCD micrographs using EMAN2 (56) or selected using a template-based particle picker in RELION 1.3 (57) from the averaged cryo-EM micrographs with 2D class averages of a small subset of manually selected particles as templates. A total of 6125 and 17 461 particles were selected from CCD micrographs for sRNP assembled with WT sR8 and di-sR8, respectively, and 164 282 particles were selected from the aligned and averaged cryo-EM micrographs for the sRNP assembled with WT sR8. Reference-free 2D classification into 200 classes was performed in RELION with CTF correction.

For 3D reconstruction of the *M. jannaschii* WT di-sRNP, 2D classes were visually inspected and low-resolution particles, aggregates and contaminants were removed and 135 635 particles were subjected to 3D classification in RELION into 4 classes, using a 60Å low-pass filtered negatively stained *M. jannaschii* sRNP EM reconstruction as reference (45). Two 3D classes were selected and merged into a final set of 72 129 particles and subjected to 3D auto-refine in RELION, yielding a 12.0Å map at 0.143 FSC. To further improve particle alignment, we utilized the alignparts_lmfgs algorithm in (58) to track and correct for beam-induced motions of individual particles. These 'polished' particles were subjected to a second round of 3D classification into 3 classes using a 60Å low-pass filtered map from the refinement of the unpolished particles as reference. Using 32 771 particles from the best class, we performed a final round of 3D auto-refine, with C2 symmetry imposed, using the corresponding class model low-pass filtered to 60Å as the starting model. The map was filtered and sharpened with post-processing in RELION using a B-factor of $-900Å^2$ to yield the final reconstruction with a resolution of 9.0Å at 0.143 FSC. Local resolution of the final reconstruction was estimated using ResMap (Supplementary Figure S1C) (59). All reported resolutions are based on the gold standard 0.143 FSC criterion using two independent half-maps.

Docking of atomic models and analysis of the EM map

Using Segger in Chimera (60), the reconstruction was segmented based on inspection of the map, rigid-body docking of available crystal structures and previous knowledge of the sRNP complex. The threshold of each segment was adjusted to reflect the local resolution of the map. To perform rigid-body docking, two copies of the co-crystal structures from *P. furiosus* [PDB ID: 3NVI, (44)], each containing two copies of L7Ae, kink-turn RNA and Nop5 lacking the NTD (amino acids 127–373) were docked as rigid bodies into the center of the volume based on prior knowledge of the location of the Nop5 coiled coil domain (44,45,48) using the Fit in Map in Chimera (60). Subsequetly, four copies of *P. furiosus* Nop5 N-terminal domain (amino acids 8–126) and fibrillarin from [PDB ID: 2NNW, (41)] were docked into the 4 corners of the volume using Fit to Segments in Chimera, without changing the relative orientation between the 2 proteins (41). To refine the docking, a simultaneous multi-fragment docking refinement was performed using Collage in Situs 2.8 (61). The two 6-base-pair A-form RNA double helices were built using Build Structure in Chimera. All images and movies of 3D volumes were created and displayed using Chimera (60,62).

RESULTS

To elucidate the orientation of the box C/D sRNAs in the di-sRNP, we used cryo-EM to determine the structure of the box C/D sRNP from *M. jannaschii*. Due to staining artifacts, the density that would represent the sRNAs cannot be resolved in previous negatively stained EM structural studies (45,48). In contrast, cryo-EM embeds the specimen in a frozen hydrated state and thus eliminates staining artifacts. Therefore, cryo-EM is the ideal method for visualizing the sRNA orientation in the box C/D di-sRNP.

Cryo-EM reveals the sRNA location in the archaeal box C/D di-sRNP

To examine the box C/D sRNP complex in cryoEM, we reconstituted the box C/D sRNP with the core proteins and the sR8 sRNA from *M. jannaschii* and purified the assembled complex using SEC (Figure 2A). The di-sRNP complex elutes from the column as a homogenous peak (theoretical molecular mass 376 kD) (Figure 2A). SDS PAGE and northern blot analysis revealed that all sRNP components co-migrated in the peak fractions (fractions 5 and 6, Figure 2B). Using peak fraction 5, we subjected the box C/D sRNP to cryo-EM examination and single particle analysis. Electron micrographs of the box C/D sRNP particles (Figure 2C) as well as the 2D class averages (Figure 2D) show that the dimensions and the overall shape of the cryo-EM sRNP particles are consistent with previous negatively stained EM images from both the same and different archaeal species (45,47,48).

To determine the orientation of the two box C/D sRNAs in the sRNP complex, we performed 3D classification and refinement of the cryo-EM single-particle images to arrive at a high-resolution 3D reconstruction of the sRNP complex. The resulting EM volume, which reaches a resolution of 9.0Å using the gold standard Fourier shell correlation (FSC) at 0.143 as a criterion (Supplementary Figure S1), has a front view and a back view (Figure 2E, Supplementary Movie 1) that show the characteristic X-shape as seen in previous negatively stain 3D reconstructions (45,48). At this resolution, several α-helices, including those in the Nop5 coiled coil domains, can be clearly visualized. Interestingly, the side view reveals a tea-cup-handle-shaped density (Figure 2E, light brown) that is absent in the negatively stained reconstructions (Supplementary Figure S2) (45,48). Since all of the EM density in a negatively stained box C/D sRNP can be occupied by the core proteins via docking of the protein crystal structures into the volume (45,48), the new, unaccounted for density in the cryo-EM reconstruction must represent the box C/D sRNAs.

To better interpret the cryo-EM volume and to determine the location of the sRNAs, we docked in crystal structures that contain the core proteins and the kink-turn RNAs (Figure 2F). One structure is a co-crystal structure containing two kink-turn RNAs, each bound to an L7Ae and one of the two CTDs of the Nop5 homodimer lacking the NTD (Nop5ΔN) [PDB ID: 3NVI, (44)]. Two copies of the co-crystal structure were docked into the volume as a whole, without altering the relative orientation among the proteins and the RNAs, to provide information about the location of the sRNAs. Although the kink-turn RNAs in the co-crystal structure are not full-length sRNAs, they serve as a visual guide to trace the path that each sRNA takes through the cryo-EM volume, as the kink-turn/kink-loop structural motif is located at either the stem end or the loop end in the secondary structure of the sRNA (Figure 1A). We docked four copies of the crystal structure containing the Nop5 NTD and fibrillarin into the remaining densities at the four corners of the di-sRNP [PDB ID: 2NNW (41)], as described in (45,48).

Docking of the crystal structures revealed two major unaccounted for densities (Figure 2F, arrowheads in side and top view). These densities likely represent sequences of the box C/D sRNA that are not present in the crystal structures: namely, the stem and the guide sequences (Figure 1A). Together with the crystal structures of the kink-turn RNAs, the presence and location of the densities suggest that the sRNAs penetrate from one face of the sRNP through the center to the other face (Figure 2E and F). This is in agreement with the previous proposal that the sRNAs run perpendicular to the coiled coil domain of Nop5 (45,48).

The box C/D sRNAs are arranged in a parallel orientation

The cryo-EM model of the *M. jannaschii* box C/D sRNP presented here is significantly different from the previously published NMR-based structural model of *P. furiosus* box C/D sRNP by (49). While the NMR structural model agrees with the general shape of the cryo-EM volume in having the characteristic X-shape in the front and back views, the location and orientation of the box C/D sRNAs differ substantially (Figure 3). In this cryo-EM model, we propose that the two sRNAs go from one face, through the center, to the other (Figure 3A and D). In contrast, in the NMR model, the sRNAs lie on only one face of the complex (Figure 3B, Front versus Back) and run as U- and upside down U-shapes (Figure 3B, D). Strikingly, when we docked the NMR-derived box C/D sRNP model (49) into our cryo-EM volume as a rigid body, we found large structural differences in the side view, particularly in a density that likely represents the sRNAs (Figure 3C). Importantly, the proposed locations of the sRNAs in the cryo-EM model can account for this density (Figure 3A).

There are four possible orientations of the two sRNAs with respect to each other in the di-sRNP. The two sRNAs either run parallel to one another where both stem ends are on the same face of the complex and the loop ends are on the other face (Parallel Orientations 1 and 2, Figure 3E), or anti-parallel to one another where the stem end of one sRNA is located on a different face from that of the other sRNA (Anti-parallel Orientations 1 and 2, Figure 3E). We propose a model in which the two sRNAs run parallel to each other in the di-sRNP with the stem ends of both sRNAs representing the tea-cup-handle-shape density and the loop ends are on the other face of the complex based on the following observations (Parallel Orientation 1, Figure 3E). First, the kink-turn RNAs in the crystal structures (3-nucleotide bulge, 2 base-pairs and 4 unpaired nucleotides), which are slightly longer than the loop end of the *M. jannaschii* box sR8 box C/D sRNA (6 unpaired nucleotides), already fully account for the RNA density exposed on the back face of the cryo-EM volume (Figures 2F and 3A). Thus, it is likely that the RNA density exposed on the back face corresponds to the loop ends of both sR8 sRNAs. Second, the stem end (3-nucleotide bulge and 8 base-pairs) of the sR8 sRNA is longer than both the loop end and the crystal structure kink-turn RNA. Therefore, the unexplained density in the front face of the cryo-EM volume (right arrow head of the side view, Figure 2F) can be accounted for by the stem ends of the two sRNAs. In fact, the unexplained density can accommodate two 6-base-pair A-form RNA with no steric clashes (purple, Figure 3A, Sup-

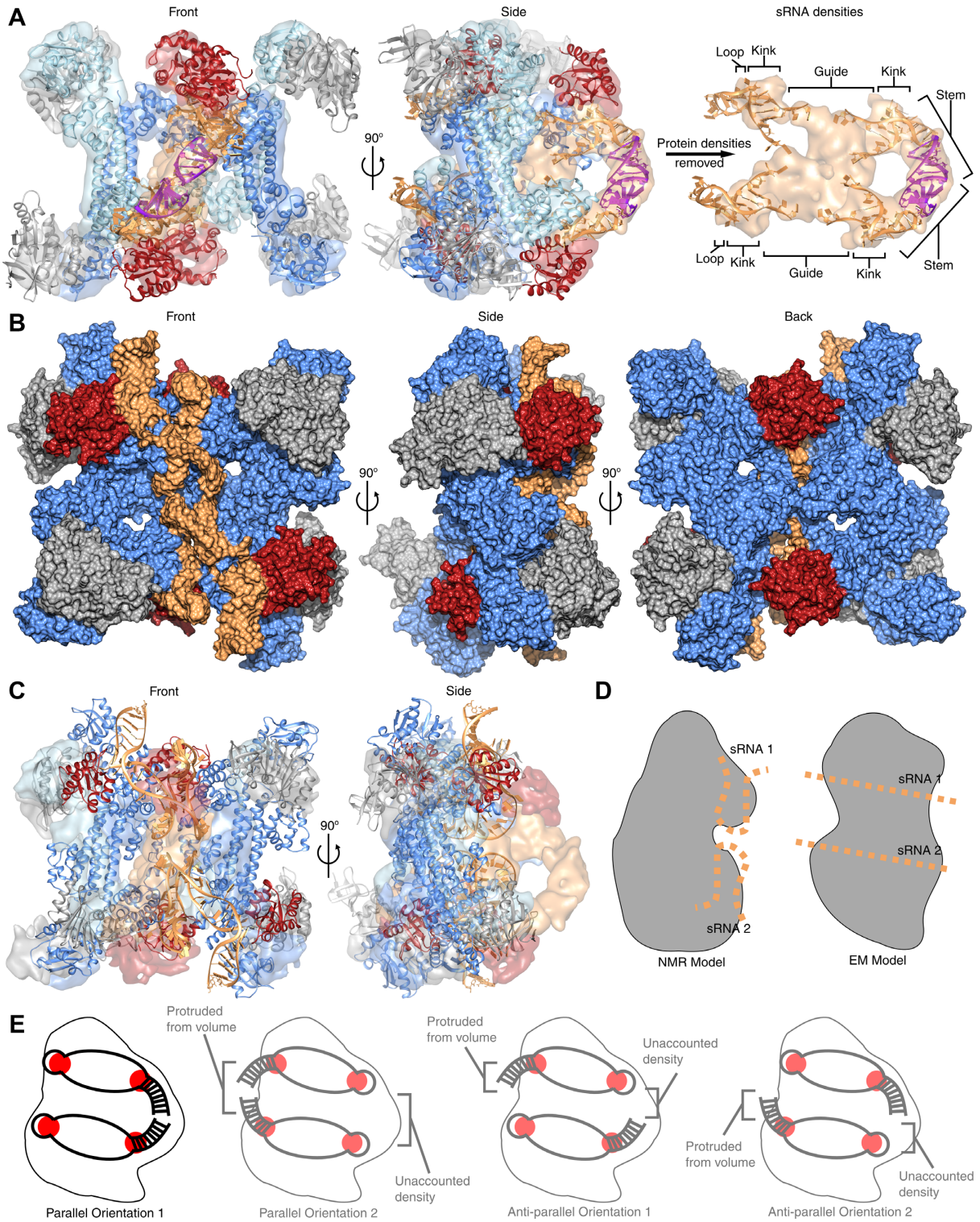

Figure 3. The cryo-EM model of *M. jannaschii* box C/D di-sRNP reveals parallel sRNA orientation. (**A**) **Left and middle panels**: front and side views of cryo-EM volume of the *M. jannaschii* box C/D di-sRNP, with two 6-base-pair A-form RNA helices (in purple) modeled into the volume. **Right panel**: side view of the cryo-EM volume, showing only the sRNA densities, with crystal structure kink-turn RNAs and the modeled A-form RNA helices docked in the densities. Different parts of the sRNAs are labeled accordingly. Color code is the same as in Figure 2E. (**B**) NMR structural model of *P. furiosus* box C/D sRNP in surface representation, determined by (49). Color code is the same as in Figure 2E, except that Nop5 is only in one shade of blue. (**C**) Docking of the NMR structural model from (49) into the cryo-EM volume. The NMR model is in ribbon representation. (**D**) A cartoon of the NMR structural model (left) and the cryo-EM structural model (right), highlighting the paths of the sRNAs. The gray shapes represent the proteins of the sRNP in each model. The light brown dotted lines represent the path of each copy of sRNA with respect to the protein density. 'sRNA 1' and 'sRNA 2' each indicate a single copy of sRNA in each model. (**E**) A schematic showing four possible orientations of box C/D sRNAs. The gray envelope outlines the EM volume in the side view. The red dots represent the locations of the 'kinks' as marked by the kink-turn RNAs from the crystal structures.

plementary Movie 1). Two 6-base-pair A-form RNA helices together with the two 2-base-pair stretches of RNA adjacent to the kinks in the crystal structure kink-turn RNAs can fully account for two 8-base-pair stem of two normal sR8 sRNAs (Figure 3A). Third, the four L7Ae proteins can clearly be visualized in the cryo-EM reconstruction with the help of the docked crystal structures. Previously published biochemical and structural studies have shown that L7Ae binds to the kink-turn and kink-loop structures (19,27,33–37). Therefore, the L7Ae proteins can act as visual markers for the location of the kink structures (red dots in Figure 3E). Since the locations of the kinks are fixed, the loop ends and the stem ends must extend from these fixed kink structures. As the stem ends are longer than the loop ends, Parallel Orientation 1 is the only possible orientation for the two sRNAs (Figure 3E). Other orientations will leave some of the tea-cup-handle-shaped density unaccounted for because the extension of one or both loop ends from the kinks is too short to occupy the entire arc of the density, and leave either one or both stem ends protruding from the EM volume (Parallel Orientation 2 and Anti-parallel Orientations 1 and 2, Figure 3E). Parallel orientation 1 places the loop ends and stem ends on the back and front faces, respectively, of the box C/D di-sRNP, with the guide sequences in the core (Figure 3A). In this orientation, the extension of the stem ends from the kink is long enough to allow one stem end to reach the other, forming the full arc of the tea-cup-handle-shaped density. Interestingly, this parallel orientation positions the stem end of each sRNA in close proximity (Parallel Orientation 1, Figure 3E).

The importance of the box C/D sRNA stem ends in di-sRNP assembly

The parallel orientation of the two box C/D sRNAs in the di-sRNP places the two stem ends of the sRNAs in close proximity (Figure 3A), suggesting a potential interaction between them. To test this hypothesis, we designed sR8 sRNA mutants that either have truncated or mismatched stem ends (Figure 4A). We predicted that disrupting the stem end of the sRNAs would disrupt stem end-to-stem end interaction between the two sRNAs and would lead to lower di-sRNP assembly efficiency. Using native PAGE, a technique that we have used previously to assess di-sRNP assembly efficiency (45,47,48), we discovered that box C/D sRNAs with disrupted stem ends assembled less efficiently into di-sRNPs (Figure 4B–D). As the stem is shortened through truncation, the di-sRNP assembles less efficiently (Figure 4B, compare lane 1 with lane 2 and 3) even with equal amount of sRNAs in the assembling reactions (Figure 4C). The same trend holds true when base-pairing of the stem was disrupted (Figure 4B, compare lane 1 with lane 4 and 5), indicating that a base-paired stem of the box C/D sRNA of a certain length is necessary for efficient di-sRNP assembly. Quantitation of the gel band intensities in triplicate verifies these results (Figure 4D). These results are consistent with the model that the two stem ends of the sRNAs in the box C/D di-sRNP are in close proximity and interact with each other when assembled into a di-sRNP.

To further probe the importance of the interaction between the stem ends of the box C/D sRNAs for di-sRNP assembly, we examined di-sRNP formation with a fusion di-sRNA by SEC, native PAGE, *in vitro* methylation activity assays and negatively stained EM. We generated the fusion di-sRNA by covalently linking one sR8 sRNA at the 5′ end to the 3′ end of another sR8 sRNA to mimic the proximity of the stem ends in the box C/D di-sRNP structure (di-sR8 sRNA in Figure 5A). We assembled the di-sR8 sRNA with the box C/D core protein components and analyzed di-sRNP assembly using SEC (Figure 5B). The sRNP peaked at an elution volume of 12.5 ml, which is very similar to the elution volume (12.4 ml) of the WT sR8 di-sRNP (Figure 2A), suggesting that the two sRNPs are very similar in terms of their sizes and their shapes. Furthermore, native PAGE analysis of the combined peak fractions (5–7) of the di-sR8 sRNP reveals that it migrates at the same position as the WT sR8 di-sRNP, indicating that the two sRNPs have very similar biochemical properties (Figure 5C).

To ask whether the two sRNPs have similar activity, we performed *in vitro* methylation activity assays (Figure 5D). To measure the activity of the sRNPs, we introduced substrate RNAs that are either complementary to the D guide (D substrate) or to the D' guide (D' substrate), and SAM, the methyl donor, which contains a tritiated (^{3}H) methyl group, to WT and to the di-sR8 sRNPs. If a sRNP is active, it will incorporate the ^{3}H-methyl group at the 2′-*O* position of the target nucleotide. We can measure the radioactivity as an indication of the amount of methyl incorporation. As a negative control, we used substrates that were pre-methylated at the 2′-*O* position of the target nucleotide, so that no ^{3}H-methyl can be incorporated. The *in vitro* methylation assays show that the di-sR8 sRNP has a significantly higher amount of ^{3}H-methyl incorporation into the un-methylated substrates than into the pre-methylated substrates. This is true for both the D and the D' substrates. This indicates that the di-sR8 sRNP is catalytically active, and is capable of methylating both D and D' substrates. Therefore, the di-sR8 sRNA permits assembly into a di-sRNP that is catalytically active.

Furthermore, we examined both WT sR8 and di-sR8 di-sRNPs from SEC purified peak fractions using negatively stained EM and 2D classification of the single-particle images. Comparison of the 2D class averages between them shows that they adopt very similar structural features and indicates that the di-sR8 sRNA allows the sRNP to adopt a di-sRNP architecture (Figure 5E). Taken together, these experiments suggest that the di-sR8 sRNP is very similar to the WT sR8 di-sRNP both biochemically and structurally. These results support the hypothesis that the two sRNAs are oriented parallel to each other with their stem ends in close proximity.

DISCUSSION

Recent biochemical and structural studies of archaeal box C/D sRNPs have established that *in vitro* assembled archaeal box C/D sRNPs assume a di-sRNP architecture. Nevertheless, the orientation of the box C/D sRNAs in a box C/D di-sRNP has remained ambiguous. Here, we present a 3D reconstruction of the *M. jannaschii* box C/D di-sRNP using cryo-EM, which reveals that the sRNA density enters from one face of the complex, passes through

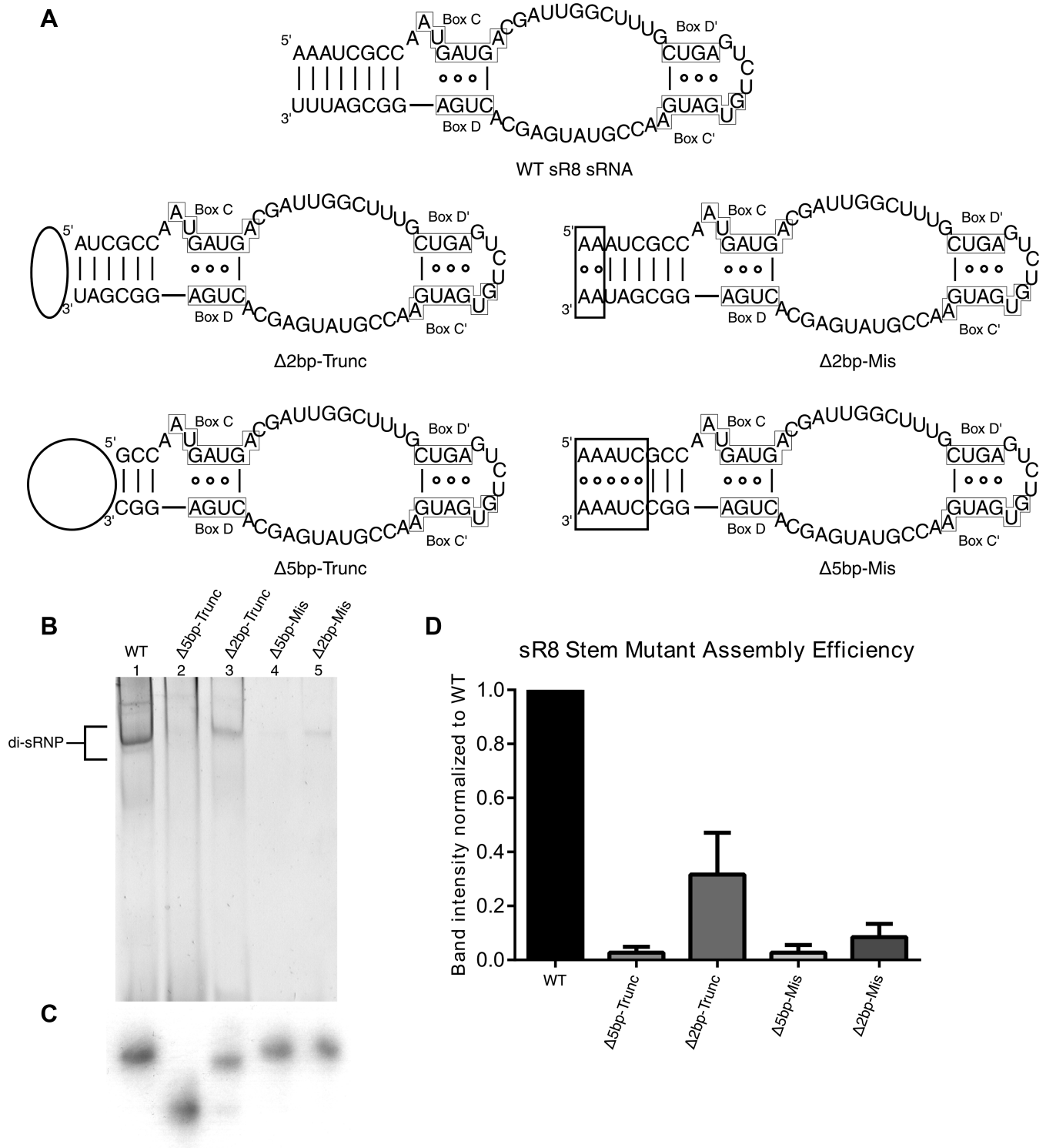

Figure 4. Box C/D sRNA stem end is important for efficient di-sRNP assembly. (**A**) Sequences and secondary structures of WT and stem end mutated box C/D sRNAs. The circles and rectangles indicate, respectively, the truncations and mismatch mutations that disrupt the stem end of box C/D sRNA. (**B**) Native PAGE analysis of box C/D di-sRNP assembled with WT and stem end mutated box C/D sRNAs. (**C**) Northern blot showing the amount of sRNAs used in the sRNP assembly in the Native PAGE in Figure 4B. (**D**) Quantitation of the gel band densities normalized to WT sR8 in triplicates. Error bars correspond to 95% confidence intervals.

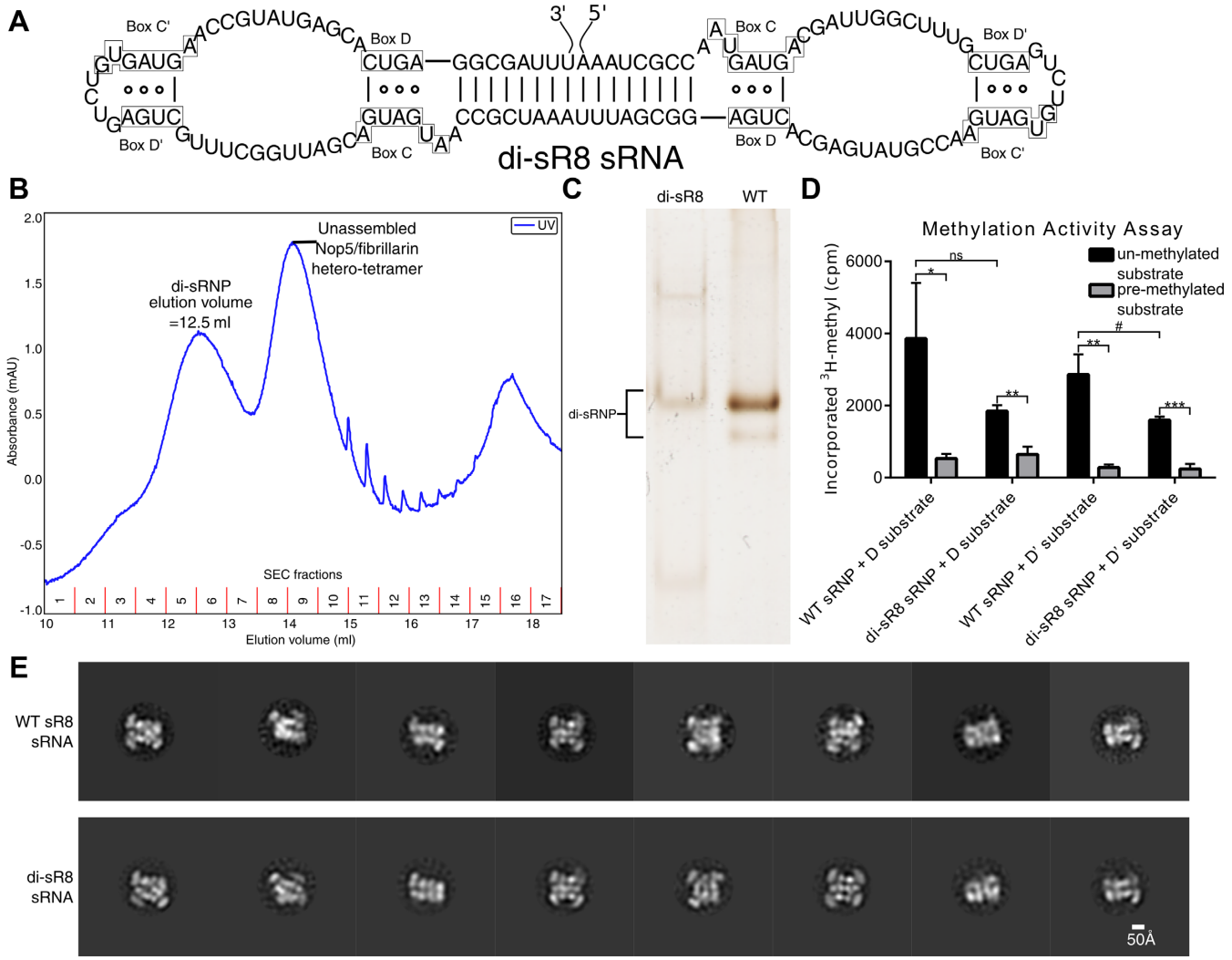

Figure 5. Fusion box C/D di-sRNA, covalently linked at stem ends, allows for the formation of a di-sRNP. (**A**) Sequence and secondary structure of stem-end fused box C/D di-sRNA. (**B**) SEC of box C/D sRNP assembled with box C/D di-sR8 sRNA. Box C/D di-sRNP elutes in fractions 5, 6 and 7, corresponding to an elution volume of 12.5 ml. The peak at elution volume of 14.1 ml corresponds to the unassembled Nop5/fibrillarin heterotetramer. (**C**) Native PAGE of box C/D sRNP assembled with di-sR8 and WT sR8 sRNAs. (**D**) Methylation activity assays of WT and di-sR8 sRNPs. Error bars correspond to one standard deviation. Asterisks (*) denote statistical significance for comparing the activity of the same sRNP using un-methylated and pre-methylated substrates. Hash marks (#) denote statistical significance for comparing the activity of WT and di-sR8 sRNPs using the un-methylated D' substrate. * or #, $P < 0.05$; **, $P < 0.01$; ***, $P < 0.001$; ns, not significant. (**E**) Comparison of the experimental 2D class averages between box C/D sRNP assembled with the WT sR8 sRNA (upper panel) and the di-sR8 sRNA (lower panel) shows that di-sR8 sRNA is capable of forming a di-sRNP. Scale bar is 50 Å.

the core, and exits to the other face. Docking of crystal structures of box C/D sRNP proteins and kink-turn RNAs into the reconstruction suggests a parallel orientation of the sRNAs. Furthermore, experiments with mutant sRNAs with disrupted stem ends and a di-sR8 fusion sRNA reveal that the stem ends of the two sRNAs are in close proximity and potentially interact to stabilize the di-sRNP structure.

How are the box C/D sRNAs oriented differently in the cryo-EM versus the NMR model?

The NMR structural model of *P. furiosus* box C/D di-sRNP from (49) suggests that the box C/D sRNAs lie as a continuous long rod on the surface of only one face of the di-sRNP complex (Figure 3B). As they do not penetrate into the core of the complex, the sRNAs run in a direction that is parallel to the Nop5 coiled coil domains. This suggests that deleting the Nop5 coiled coil domains would still allow the formation of a di-sRNP structure as the top and bottom half of the sRNP complex would be tethered together by the sRNA interface. However, biochemical evidence indicates that a di-sRNP is unable to form when the complex lacks the Nop5 coiled coil domains, arguing against the sRNA orientation proposed in the NMR model (45).

In contrast, the sRNA orientation presented here based on the *M. jannaschii* box C/D di-sRNP cryo-EM structure is consistent with previous biochemical evidence. In the cryo-EM model, both box C/D sRNAs penetrate through the core of the box C/D sRNP complex with the stem ends and the loop ends of the sRNAs exposed on the front and

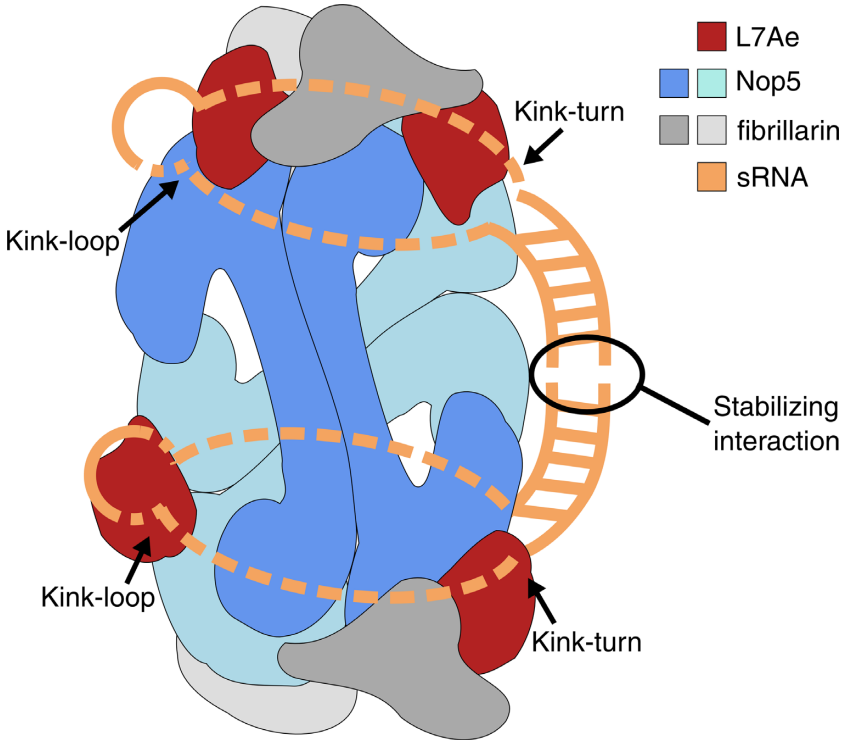

Figure 6. A model of box C/D sRNA orientation in the box C/D sRNP. The stem ends of the two box C/D sRNAs orient adjacent to each other and they interact with each other to stabilize the di-sRNP architecture. Arrows indicate the locations of the kink-turns and kink-loops of the sRNAs. The color key of the proteins and the sRNAs are indicated in the upper right corner.

back faces of the di-sRNP, respectively. The sRNAs are therefore perpendicular to the Nop5 coiled coil domains. This is consistent with previous results that indicate that the box C/D and C'/D' elements as well as the Nop5 coiled coil domains are necessary for the formation of the di-sRNP (36,44–47). The sRNAs provide an interface that bridges the left half of the di-sRNP complex (front or back view) with the right half, while the Nop5 coiled coils provide an interface that bridges the top half with the bottom half (Supplementary Figure S3) (47). Therefore, both the sRNA interface and Nop5 coiled coil domain interface are equally important in the maintenance of the di-sRNP architecture.

Moreover, there are further inconsistencies in the placement of the box C/D sRNA stem ends in the NMR model. In the NMR model, the stem ends of the box C/D sRNAs are located at the opposite extremes of the sRNP complex. However, experiments presented here with mutant sRNAs and a fusion di-sRNA strongly suggest that the stem ends of the two box C/D sRNAs are in close proximity (Figures 4 and 5), arguing against this placement. In contrast, the parallel arrangement of the box C/D sRNAs in the cryo-EM model allows the sRNA stem ends to be in close proximity. All in all, the sRNA orientation in the cryo-EM model presented here is consistent with current and previous published biochemical results, while the NMR model is not.

There are several possibilities as to why the NMR model resulted in mis-placement of the box C/D sRNAs (49). First, the sRNA used for sRNP assembly was altered from the WT sRNA in a critical manner. An insertion of a 4 base-pair stem in between the box C'/D' element and the loop end region was made in the sRNA used in the NMR model. This would effectively modify the kink-loop structure normally found in the archaeal box C/D sRNA into a kink-turn structure (27–31). As it has been shown previously, the presence of the kink-loop structure is absolutely essential for the maintenance of the di-sRNP architecture (48). Therefore, changing the kink-loop structure of the box C/D sRNA into a kink-turn structure in the NMR model has likely changed the interaction of L7Ae and the Nop5 CTD with the box C'/D' elements of the sRNA and forced the sRNAs to be abnormally oriented.

Second, the structural determination of the NMR model was not entirely *de novo*. Because of the large size of an archaeal box C/D sRNP (~400 kD), it is technically challenging to use NMR as a sole method for structural determination. Instead, Lapinaite *et al.* (49) relied on published crystal structures [PDB ID 3NMU, (44)] that contain pieces of the complete box C/D sRNP to aid in structural determination together with the new NMR and small-angle neutron scattering (SANS) measurements. One assumption that was made to obtain the NMR model was that the relative orientations between L7Ae and the kink-turn RNA and between fibrillarin and Nop5 in the crystal structures of pieces of the di-sRNP are conserved in the complete box C/D di-sRNP. An additional assumption was that the L7Ae-kink-turn-RNA-Nop5-CTD interface and the Nop5-NTD-fibrillarin interface are also conserved. A solution of the box C/D sRNP structure was calculated based on NMR and SANS data that provided information on how these conserved modules orient with respect to each other in the di-sRNP

environment. This method, while elegant, did not generate a *de novo* density map of the complete box C/D di-sRNP structure. In contrast, using cryo-EM, we generated a density map of the complete box C/D di-sRNP based purely on the electron scattering of the atoms in the box C/D di-sRNP. Therefore, it is likely that the bias introduced by assuming conserved crystal structure interfaces in the NMR structural calculation led to a different orientation of the sRNAs than what we have obtained in the cryo-EM model.

Finally, the use of box C/D sRNP components from different archaeal species may have also contributed to the differences in the NMR and cryo-EM derived di-sRNP structures.

The apo box C/D sRNP is not in a catalytic productive conformation

The *M. jannaschii* cryo-EM structural model of the box C/D di-sRNP reveals that the apo di-sRNP, where no substrate is bound, is not in a catalytically productive conformation (Figure 3A). In the apo di-sRNP structure, the fibrillarin proteins, which are the catalytic components of the di-sRNP, are located far from the guide sequences of the box C/D sRNAs, which are the binding sites of the substrate. This implies that one or more fibrillarin proteins must undergo large conformational changes to reach the substrate bound to the guide sequences, as seen in (49). Indeed, local resolution estimation of the cryo-EM model shows that the fibrillarin proteins have lower resolution compared to the rest of the complex, which suggests that they are flexible, consistent with potentially large movements (Supplementary Figure S1C). Moreover, published X-ray crystallographic and mutational analysis of the Nop5-fibrillarin hetero-tetramer have suggested that there is a flexible hinge in the Nop5 NTD that allows major rearrangements of the Nop5 NTD and its associated fibrillarin (39,41,44). These lines of evidence suggest that binding of the substrate induces large conformational changes in the positions of the catalytic fibrillarin proteins. Whether the box C/D di-sRNP requires the binding of one or more substrates at the guide sequences to achieve the catalytically productive conformation requires further investigation.

Interestingly, the guide sequences of the box C/D sRNAs in the apo box C/D di-sRNP are located within the core of the complex. The solvent exposed regions of the guide sequences are accessible from the top and bottom of the sRNP complex (Figure 3A). Therefore, it is plausible that the substrate RNA threads through the hole on either the top or bottom of the complex, thereby reaching the entirety of the guide sequences, and allowing base-pairing interactions between the substrate and the guide sequences. Intriguingly, recent studies have shown that the D' substrate has a higher turnover rate than the D substrate (63). Based on our cryo-EM model, it is possible that the D' guide sequences are closer to the top and bottom of the di-sRNP, while the D guide sequences are located more in the core of the complex. Unfortunately, at the current resolution of the cryo-EM structure, it is not possible to distinguish between the identities of the D and D' guide sequences.

Stem end interactions of box C/D sRNA stabilize the sRNP complex

This study of the *M. jannaschii* box C/D di-sRNP not only demonstrates that the two box C/D sRNAs are arranged in a parallel fashion, but also suggests that the stem ends of the sRNAs are close to each other and are likely interacting in some way (Figure 6). The experiments with the di-sR8 sRNA showed that the fusion di-sRNA was capable of assembling into a catalytically active di-sRNP that is structurally indistinguishable from the WT sRNA di-sRNP. This suggests that the stem ends of the two sRNAs are normally in close proximity and likely interact with each other to stabilize the di-sRNP architecture (Figure 6). The decreasing efficiency of box C/D sRNP assembly as a result of the disruption of the box C/D sRNA stem ends (Figure 4) provided further support for this notion. Interestingly, di-sRNP assembled with the fusion di-sRNA has lower activity than the WT sRNA with both the D (not statistically significant) and D' (statistically significant) substrates (Figure 5D). It is therefore tempting to speculate that flexibility around the point of the proposed stem end-to-stem end interaction is necessary for efficient catalysis, because fusing the stems in the di-sRNA would make that area more rigid. Local resolution estimation of the box C/D di-sRNP cryo-EM structure (Supplementary Figure S1C) reveals that the structure has a lower resolution around the point of the proposed stem end-to-stem end interaction. This is consistent with a flexible stem end-to-stem end contact. Whether this flexibility is necessary for catalysis requires further experimentation.

Combining this study with previously published work reveals that we have identified three regions of a box C/D sRNA that are essential for the formation of a di-sRNP: (1) the box C/D kink-turn elements and (2) the box C'/D' kink-loop elements for tethering the left and right halves of the box C/D sRNP components, and (3) the sRNA stem ends that confer a stabilizing interaction (36,45,47,48). This suggests that the box C/D sRNA itself is critical for determining the structure of the box C/D sRNP, as both the loop ends (48) and the stem ends (this work) are required for the structural architecture of the di-sRNP. Intriguingly, not all archaeal box C/D sRNAs, predicted or verified, contain canonically base-paired terminal stems ((20–26) http://lowelab.ucsc.edu/snoRNAdb/). Among those that do not have a terminal stem, many have nucleotides that flank the box C and D sequences. It will be interesting to investigate whether these flanking nucleotides have similar interactions as those we have described here and whether they confer stability to the box C/D di-sRNP architecture.

ACCESSION NUMBERS

The 3D EM volume in this study has been deposited into EMDB (https://www.ebi.ac.uk/pdbe/emdb/). The accession ID is EMD-8146.

SUPPLEMENTARY DATA

Supplementary Data are available at NAR Online.

ACKNOWLEDGEMENTS

The authors thank E. Nogales (University of California, Berkeley) and H-W. Wang (Tsinghua University) for guidance in cryo-EM reconstruction; J. Steitz (Yale University) for experiment ideas; T. Carlomagno (European Molecular Biology Laboratory) for providing the atomic coordinates of the NMR box C/D di-sRNP model; and current and former members of the laboratories of C. Sindelar and S. Baserga for technical assistance, helpful discussions and critical reading of this manuscript. The authors thank the staff in the Yale Center for Cellular and Molecular Imaging and High-Performance Computing facility for their maintenance of these facilities.

FUNDING

D.W.T. is a Damon Runyon Fellow of the Damon Runyon Cancer Research Foundation [DRG-2218-15]; JSPS KAKESHI [15H01656 to H.S. in part]; NIH [R01 GM115710 to S.J.B]. Funding for open access charge: NIH [R01 GM115710].

Conflict of interest statement. None declared.

REFERENCES

1. Decatur,W.A. and Fournier,M.J. (2002) rRNA modifications and ribosome function. *Trends Biochem. Sci.*, **27**, 344–351.
2. Liang,X.H., Liu,Q. and Fournier,M.J. (2009) Loss of rRNA modifications in the decoding center of the ribosome impairs translation and strongly delays pre-rRNA processing. *RNA*, **15**, 1716–1728.
3. Liu,B., Liang,X.H., Piekna-Przybylska,D., Liu,Q. and Fournier,M.J. (2008) Mis-targeted methylation in rRNA can severely impair ribosome synthesis and activity. *RNA Biol.*, **5**, 249–254.
4. Liang,X.H., Liu,Q. and Fournier,M.J. (2007) rRNA modifications in an intersubunit bridge of the ribosome strongly affect both ribosome biogenesis and activity. *Mol. Cell*, **28**, 965–977.
5. Decatur,W.A., Liang,X.H., Piekna-Przybylska,D. and Fournier,M.J. (2007) Identifying effects of snoRNA-guided modifications on the synthesis and function of the yeast ribosome. *Methods Enzymol.*, **425**, 283–316.
6. Ziesche,S.M., Omer,A.D. and Dennis,P.P. (2004) RNA-guided nucleotide modification of ribosomal and non-ribosomal RNAs in Archaea. *Mol. Microbiol.*, **54**, 980–993.
7. Tollervey,D., Lehtonen,H., Jansen,R., Kern,H. and Hurt,E.C. (1993) Temperature-sensitive mutations demonstrate roles for yeast fibrillarin in pre-rRNA processing, pre-rRNA methylation, and ribosome assembly. *Cell*, **72**, 443–457.
8. Zebarjadian,Y., King,T., Fournier,M.J., Clarke,L. and Carbon,J. (1999) Point mutations in yeast CBF5 can abolish in vivo pseudouridylation of rRNA. *Mol. Cell. Biol.*, **19**, 7461–7472.
9. Higa-Nakamine,S., Suzuki,T., Uechi,T., Chakraborty,A., Nakajima,Y., Nakamura,M., Hirano,N., Suzuki,T. and Kenmochi,N. (2012) Loss of ribosomal RNA modification causes developmental defects in zebrafish. *Nucleic Acids Res.*, **40**, 391–398.
10. Decatur,W.A. and Fournier,M.J. (2003) RNA-guided nucleotide modification of ribosomal and other RNAs. *J. Biol. Chem.*, **278**, 695–698.
11. Lapeyre,B. (2005) Conserved ribosomal RNA modification and their putative roles in ribosome biogenesis and translation. *Fine-tuning RNA Funct. Modifi. Editing*, **12**, 85–91.
12. Ofengand,J. and Bakin,A. (1997) Mapping to nucleotide resolution of pseudouridine residues in large subunit ribosomal RNAs from representative eukaryotes, prokaryotes, archaebacteria, mitochondria and chloroplasts. *J. Mol. Biol.*, **266**, 246–268.
13. Maden,B.E., Corbett,M.E., Heeney,P.A., Pugh,K. and Ajuh,P.M. (1995) Classical and novel approaches to the detection and localization of the numerous modified nucleotides in eukaryotic ribosomal RNA. *Biochimie*, **77**, 22–29.
14. Del Campo,M., Kaya,Y. and Ofengand,J. (2001) Identification and site of action of the remaining four putative pseudouridine synthases in Escherichia coli. *RNA*, **7**, 1603–1615.
15. Noon,K.R., Bruenger,E. and McCloskey,J.A. (1998) Posttranscriptional modifications in 16S and 23S rRNAs of the archaeal hyperthermophile Sulfolobus solfataricus. *J. Bacteriol.*, **180**, 2883–2888.
16. Kiss-Laszlo,Z., Henry,Y., Bachellerie,J.P., Caizergues-Ferrer,M. and Kiss,T. (1996) Site-specific ribose methylation of preribosomal RNA: a novel function for small nucleolar RNAs. *Cell*, **85**, 1077–1088.
17. Nicoloso,M., Qu,L.H., Michot,B. and Bachellerie,J.P. (1996) Intron-encoded, antisense small nucleolar RNAs: the characterization of nine novel species points to their direct role as guides for the 2'-O-ribose methylation of rRNAs. *J. Mol. Biol.*, **260**, 178–195.
18. Tycowski,K.T., Smith,C.M., Shu,M.D. and Steitz,J.A. (1996) A small nucleolar RNA requirement for site-specific ribose methylation of rRNA in Xenopus. *Proc. Natl. Acad. Sci. U.S.A.*, **93**, 14480–14485.
19. Omer,A.D., Ziesche,S., Ebhardt,H. and Dennis,P.P. (2002) In vitro reconstitution and activity of a C/D box methylation guide ribonucleoprotein complex. *Proc. Natl. Acad. Sci. U.S.A.*, **99**, 5289–5294.
20. Omer,A.D., Lowe,T.M., Russell,A.G., Ebhardt,H., Eddy,S.R. and Dennis,P.P. (2000) Homologs of small nucleolar RNAs in Archaea. *Science*, **288**, 517–522.
21. Klein,R.J., Misulovin,Z. and Eddy,S.R. (2002) Noncoding RNA genes identified in AT-rich hyperthermophiles. *Proc. Natl. Acad. Sci. U.S.A.*, **99**, 7542–7547.
22. Gaspin,C., Cavaille,J., Erauso,G. and Bachellerie,J.P. (2000) Archaeal homologs of eukaryotic methylation guide small nucleolar RNAs: lessons from the Pyrococcus genomes. *J. Mol. Biol.*, **297**, 895–906.
23. Tang,T.H., Bachellerie,J.P., Rozhdestvensky,T., Bortolin,M.L., Huber,H., Drungowski,M., Elge,T., Brosius,J. and Huttenhofer,A. (2002) Identification of 86 candidates for small non-messenger RNAs from the archaeon Archaeoglobus fulgidus. *Proc. Natl. Acad. Sci. U.S.A.*, **99**, 7536–7541.
24. Tang,T.H., Polacek,N., Zywicki,M., Huber,H., Brugger,K., Garrett,R., Bachellerie,J.P. and Huttenhofer,A. (2005) Identification of novel non-coding RNAs as potential antisense regulators in the archaeon Sulfolobus solfataricus. *Mol. Microbiol.*, **55**, 469–481.
25. Zago,M.A., Dennis,P.P. and Omer,A.D. (2005) The expanding world of small RNAs in the hyperthermophilic archaeon Sulfolobus solfataricus. *Mol. Microbiol.*, **55**, 1812–1828.
26. Richter,H., Mohr,S. and Randau,L. (2013) C/D box sRNA, CRISPR RNA and tRNA processing in an archaeon with a minimal fragmented genome. *Biochem. Soc. Trans.*, **41**, 411–415.
27. Moore,T., Zhang,Y., Fenley,M.O. and Li,H. (2004) Molecular basis of box C/D RNA-protein interactions; cocrystal structure of archaeal L7Ae and a box C/D RNA. *Structure*, **12**, 807–818.
28. Klein,D.J., Schmeing,T.M., Moore,P.B. and Steitz,T.A. (2001) The kink-turn: a new RNA secondary structure motif. *EMBO J.*, **20**, 4214–4221.
29. Watkins,N.J., Segault,V., Charpentier,B., Nottrott,S., Fabrizio,P., Bachi,A., Wilm,M., Rosbash,M., Branlant,C. and Luhrmann,R. (2000) A common core RNP structure shared between the small nucleoar box C/D RNPs and the spliceosomal U4 snRNP. *Cell*, **103**, 457–466.
30. Vidovic,I., Nottrott,S., Hartmuth,K., Luhrmann,R. and Ficner,R. (2000) Crystal structure of the spliceosomal 15.5kD protein bound to a U4 snRNA fragment. *Mol. Cell*, **6**, 1331–1342.
31. Nolivos,S., Carpousis,A.J. and Clouet-d'Orval,B. (2005) The K-loop, a general feature of the Pyrococcus C/D guide RNAs, is an RNA structural motif related to the K-turn. *Nucleic Acids Res.*, **33**, 6507–6514.
32. Cavaille,J., Nicoloso,M. and Bachellerie,J.P. (1996) Targeted ribose methylation of RNA in vivo directed by tailored antisense RNA guides. *Nature*, **383**, 732–735.
33. Kuhn,J.F., Tran,E.J. and Maxwell,E.S. (2002) Archaeal ribosomal protein L7 is a functional homolog of the eukaryotic 15.5kD/Snu13p snoRNP core protein. *Nucleic Acids Res.*, **30**, 931–941.
34. Rozhdestvensky,T.S., Tang,T.H., Tchirkova,I.V., Brosius,J., Bachellerie,J.P. and Huttenhofer,A. (2003) Binding of L7Ae protein to the K-turn of archaeal snoRNAs: a shared RNA binding motif for C/D and H/ACA box snoRNAs in Archaea. *Nucleic Acids Res.*, **31**, 869–877.

35. Rashid,R., Aittaleb,M., Chen,Q., Spiegel,K., Demeler,B. and Li,H. (2003) Functional requirement for symmetric assembly of archaeal box C/D small ribonucleoprotein particles. *J. Mol. Biol.*, **333**, 295–306.
36. Tran,E.J., Zhang,X. and Maxwell,E.S. (2003) Efficient RNA 2'-O-methylation requires juxtaposed and symmetrically assembled archaeal box C/D and C'/D' RNPs. *EMBO J.*, **22**, 3930–3940.
37. Charron,C., Manival,X., Clery,A., Senty-Segault,V., Charpentier,B., Marmier-Gourrier,N., Branlant,C. and Aubry,A. (2004) The archaeal sRNA binding protein L7Ae has a 3D structure very similar to that of its eukaryal counterpart while having a broader RNA-binding specificity. *J. Mol. Biol.*, **342**, 757–773.
38. Wang,H., Boisvert,D., Kim,K.K., Kim,R. and Kim,S.H. (2000) Crystal structure of a fibrillarin homologue from Methanococcus jannaschii, a hyperthermophile, at 1.6 A resolution. *EMBO J.*, **19**, 317–323.
39. Aittaleb,M., Rashid,R., Chen,Q., Palmer,J.R., Daniels,C.J. and Li,H. (2003) Structure and function of archaeal box C/D sRNP core proteins. *Nat. Struct. Biol.*, **10**, 256–263.
40. Aittaleb,M., Visone,T., Fenley,M.O. and Li,H. (2004) Structural and thermodynamic evidence for a stabilizing role of Nop5p in S-adenosyl-L-methionine binding to fibrillarin. *J. Biol. Chem.*, **279**, 41822–41829.
41. Oruganti,S., Zhang,Y., Li,H., Robinson,H., Terns,M.P., Terns,R.M., Yang,W. and Li,H. (2007) Alternative conformations of the archaeal Nop56/58-fibrillarin complex imply flexibility in box C/D RNPs. *J. Mol. Biol.*, **371**, 1141–1150.
42. Lin,J., Lai,S., Jia,R., Xu,A., Zhang,L., Lu,J. and Ye,K. (2011) Structural basis for site-specific ribose methylation by box C/D RNA protein complexes. *Nature*, **469**, 559–563.
43. Ye,K., Jia,R., Lin,J., Ju,M., Peng,J., Xu,A. and Zhang,L. (2009) Structural organization of box C/D RNA-guided RNA methyltransferase. *Proc. Natl. Acad. Sci. U.S.A.*, **106**, 13808–13813.
44. Xue,S., Wang,R., Yang,F., Terns,R.M., Terns,M.P., Zhang,X., Maxwell,E.S. and Li,H. (2010) Structural basis for substrate placement by an archaeal box C/D ribonucleoprotein particle. *Mol. Cell*, **39**, 939–949.
45. Bleichert,F., Gagnon,K.T., Brown,B.A. 2nd, Maxwell,E.S., Leschziner,A.E., Unger,V.M. and Baserga,S.J. (2009) A dimeric structure for archaeal box C/D small ribonucleoproteins. *Science*, **325**, 1384–1387.
46. Zhang,X., Champion,E.A., Tran,E.J., Brown,B.A. 2nd, Baserga,S.J. and Maxwell,E.S. (2006) The coiled-coil domain of the Nop56/58 core protein is dispensable for sRNP assembly but is critical for archaeal box C/D sRNP-guided nucleotide methylation. *RNA*, **12**, 1092–1103.
47. Bleichert,F. and Baserga,S.J. (2010) Dissecting the role of conserved box C/D sRNA sequences in di-sRNP assembly and function. *Nucleic Acids Res.*, **38**, 8295–8305.
48. Bower-Phipps,K.R., Taylor,D.W., Wang,H.W. and Baserga,S.J. (2012) The box C/D sRNP dimeric architecture is conserved across domain Archaea. *RNA*, **18**, 1527–1540.
49. Lapinaite,A., Simon,B., Skjaerven,L., Rakwalska-Bange,M., Gabel,F. and Carlomagno,T. (2013) The structure of the box C/D enzyme reveals regulation of RNA methylation. *Nature*, **502**, 519–523.
50. Ghalei,H., Hsiao,H.H., Urlaub,H., Wahl,M.C. and Watkins,N.J. (2010) A novel Nop5-sRNA interaction that is required for efficient archaeal box C/D sRNP formation. *RNA*, **16**, 2341–2348.
51. Jinek,M., Jiang,F., Taylor,D.W., Sternberg,S.H., Kaya,E., Ma,E., Anders,C., Hauer,M., Zhou,K., Lin,S. *et al.* (2014) Structures of Cas9 endonucleases reveal RNA-mediated conformational activation. *Science*, **343**, 1247997.
52. Staals,R.H., Zhu,Y., Taylor,D.W., Kornfeld,J.E., Sharma,K., Barendregt,A., Koehorst,J.J., Vlot,M., Neupane,N., Varossieau,K. *et al.* (2014) RNA targeting by the type III-A CRISPR-Cas Csm complex of Thermus thermophilus. *Mol. Cell*, **56**, 518–530.
53. Hochstrasser,M.L., Taylor,D.W., Bhat,P., Guegler,C.K., Sternberg,S.H., Nogales,E. and Doudna,J.A. (2014) CasA mediates Cas3-catalyzed target degradation during CRISPR RNA-guided interference. *Proc. Natl. Acad. Sci. U.S.A.*, **111**, 6618–6623.
54. Shigematsu,H. and Sigworth,F.J. (2013) Noise models and cryo-EM drift correction with a direct-electron camera. *Ultramicroscopy*, **131**, 61–69.
55. Mindell,J.A. and Grigorieff,N. (2003) Accurate determination of local defocus and specimen tilt in electron microscopy. *J. Struct. Biol.*, **142**, 334–347.
56. Tang,G., Peng,L., Baldwin,P.R., Mann,D.S., Jiang,W., Rees,I. and Ludtke,S.J. (2007) EMAN2: an extensible image processing suite for electron microscopy. *J. Struct. Biol.*, **157**, 38–46.
57. Scheres,S.H. (2012) RELION: implementation of a Bayesian approach to cryo-EM structure determination. *J. Struct. Biol.*, **180**, 519–530.
58. Rubinstein,J.L. and Brubaker,M.A. (2015) Alignment of cryo-EM movies of individual particles by optimization of image translations. *J. Struct. Biol.*, **192**, 188–195.
59. Kucukelbir,A., Sigworth,F.J. and Tagare,H.D. (2014) Quantifying the local resolution of cryo-EM density maps. *Nat. Methods*, **11**, 63–65.
60. Pettersen,E.F., Goddard,T.D., Huang,C.C., Couch,G.S., Greenblatt,D.M., Meng,E.C. and Ferrin,T.E. (2004) UCSF Chimera–a visualization system for exploratory research and analysis. *J. Comput. Chem.*, **25**, 1605–1612.
61. Birmanns,S., Rusu,M. and Wriggers,W. (2011) Using Sculptor and Situs for simultaneous assembly of atomic components into low-resolution shapes. *J. Struct. Biol.*, **173**, 428–435.
62. Sanner,M.F., Olson,A.J. and Spehner,J.C. (1996) Reduced surface: an efficient way to compute molecular surfaces. *Biopolymers*, **38**, 305–320.
63. Graziadei,A., Masiewicz,P., Lapinaite,A. and Carlomagno,T. (2016) Archaea box C/D enzymes methylate two distinct substrate rRNA sequences with different efficiency. *RNA*, **22**, 764–772.